Article

Generation of a Mouse Model Lacking the Non-Homologous End-Joining Factor Mri/Cyren

Sergio Castañeda-Zegarra [1,2,5], Camilla Huse [1,2,5], Øystein Røsand [1,2,5], Antonio Sarno [1,2], Mengtan Xing [1,2], Raquel Gago-Fuentes [1,2], Qindong Zhang [1,2], Amin Alirezaylavasani [1,2], Julia Werner [1,2,3], Ping Ji [1], Nina-Beate Liabakk [1], Wei Wang [1], Magnar Bjørås [1,2], Valentyn Oksenych [1,2,4,*]

[1] Department of Clinical and Molecular Medicine (IKOM), Norwegian University of Science and technology, 7491 Trondheim, Norway; sergio.m.c.zegarra@ntnu.no (S.CZ.); camilhus@stud.ntnu.no (C.H.); oystein.rosand@ntnu.no (Ø.R.); antonio.sarno@ntnu.no (A.S.); mengtan.xing@ntnu.no (MT.X.); raquel.gago-fuentes@ntnu.no (R.GF.); qindongz@stud.ntnu.no (Q.Z.); aminalir@stud.ntnu.no (A.L.); ping.ji@ntnu.no (P.J.); nina.beate.liabakk@ntnu.no (NB.L.); wei.wang@ntnu.no (W.W.); magnar.bjoras@ntnu.no (M.B.); valentyn.oksenych@ntnu.no (V.O.)

[2] St. Olavs Hospital, Trondheim University Hospital, Clinic of Medicine, Postboks 3250 Sluppen, 7006 Trondheim;

[3] Heidelberg University, Heidelberg, Germany; julia.werner@stud.uni-heidelberg.de (J.W.)

[4] Department of Biosciences and Nutrition (BioNut), Karolinska Institutet, 14183 Huddinge, Sweden (V.O.)

[5] These authors contributed equally (S.CZ.); (C.H.); (Ø.R.)

* Correspondence: valentyn.oksenych@ntnu.no;

Abstract: Classical non-homologous end joining (NHEJ) is a molecular pathway that detects, processes and ligates DNA double-strand breaks (DSBs) throughout the cell cycle. Mutations in several NHEJ genes result in neurological abnormalities and immunodeficiency both in humans and mice. The NHEJ pathway is required for the V(D)J recombination in developing B and T lymphocytes, and for class switch recombination in mature B cells. Ku heterodimer formed by Ku70 and Ku80 recognizes DSBs and facilitates recruitment of accessory factors (e.g., DNA-PKcs, Artemis, Paxx and Mri/Cyren) and downstream core factors subunits XLF, XRCC4 and Lig4. Accessory factors might be dispensable for the process depending on the genetic background and DNA lesion type. To determine the physiological role of Mri in DNA repair and development, we introduced frame-shift mutation in the Mri gene in mice. We then analyzed development of *Mri*-deficient mice as well as wild type and immunodeficient controls. Mice lacking Mri possessed reduced levels of class switch recombination in B lymphocytes and slow proliferation of neuronal progenitors when compared to wild type littermates. Human cell lines lacking Mri were as sensitive to DSBs as WT controls. Overall, we concluded that Mri/Cyren is largely dispensable for DNA repair and mouse development.

Keywords: NHEJ; double-strand breaks; mouse model; lymphocyte; neurodevelopment

1. Introduction

Non-homologous end-joining (NHEJ) is a molecular pathway that recognizes, processes and repairs DNA double-strand breaks (DSBs) throughout the cell cycle [1]. Core NHEJ factors Ku70 and Ku80 form heterodimer (Ku) that is rapidly associated with the DSB sites facilitating recruitment of downstream factors, including core X-ray cross-complementing 4 (XRCC4) and DNA ligase 4 (Lig4). XRCC4-like factor (XLF) is also a core factor that binds XRCC4 and stimulates Lig4-dependent DNA ligation. A number of accessory NHEJ factors are required for specific DNA end processing and DNA complex stabilization, i.e. DNA-dependent protein kinase, catalytic subunit (DNA-PKcs), nuclease Artemis, and structural components, a paralogue of XRCC4 and XLF (PAXX) and modulator of retroviral infection (Mri) [2, 3]. Mice lacking Ku70, Ku80, DNA-PKcs or Artemis possess severe combined immunodeficient phenotype (SCID), while inactivation of both alleles of *Xlf* gene results

in 2-3 folds reduced B and T cell count [4-8]. Mice lacking PAXX or Mri possess no or very modest phenotype due to functional redundancy with XLF [9-13]. Contrary, mice lacking either XRCC4 or Lig4 demonstrate p53- and Ku-dependent embryonic lethality, which correlates with massive neuronal apoptosis in central nervous system [1, 14-18].

Combined inactivation of *Xlf* and *Dna-pkcs* results in p53- and Ku70-dependent perinatal lethality in mice [11, 19, 20]. Moreover, deficiency or haploinsufficiency for *Trp53* rescues synthetic lethality between *Xlf* and *Paxx* [11]. XLF is also functionally redundant in mouse development with Mri [21], recombination activating gene 2, RAG2 [22], and a number of DNA damage response (DDR) factors, including Ataxia telangiectasia mutated (ATM) [7], histone H2AX [7, 23], Mediator of DNA damage checkpoint protein 1 (MDC1) [11], and p53-binding factor (53BP1) [8, 24].

Development of B and T lymphocytes depends on programmed DSBs induced by RAG during the V(D)J recombination, and NHEJ pathway, which is used for error-prone DNA repair [4]. Moreover, mature B cells replace constant regions of immunoglobulins during the somatic recombination process known as class switch recombination (CSR), when DSBs are initiated by activation-induced cytidine deaminase (AID) and Uridine-N-glycosylase (UNG), and NHEJ is used for DNA repair [1, 25, 26]. Furthermore, the NHEJ process is required for neurodevelopment by preventing neuronal apoptosis [1, 27].

Mri was initially described as an *open reading frame at human chromosome 7 (C7orf49)*, a factor reversing the resistance to retroviral infection in cell lines [28]. Mri was found to enhance NHEJ [29] and possess an N-terminal Ku-binding motif (KBM) [30]. Later, Mri/Cyren was suggested to inhibit NHEJ at telomeres during the S and G2 phases of the cell cycle [31], and finally confirmed to be a *bona fide* NHEJ factor, which is functionally redundant with XLF in mouse development, including the V(D)J recombination and development of central nervous system [21]. However, it was not clear whether XLF and Mri functionally overlap during the early stages of neurodevelopment, e.g. supporting proliferation and self-renewal of neuronal stem cells. Moreover, due to the lack of viable mouse model deficient for both XLF and Mri, impact of Mri on B and T lymphocyte development *in vivo* is not fully understood.

Here, we introduced a frame-shift mutation to *exon 2* of the murine *Mri* gene. By interbreeding heterozygous parents, we obtained $Mri^{-/-}$, $Mri^{+/-}$ and $Mri^{+/+}$ mice at nearly expected ratios. Mri-deficient mice possessed normal body size and number of B and T lymphocytes; however, we detected that stimulated primary mature $Mri^{-/-}$ B cells had reduced levels of IgG1, and $Mri^{-/-}$ neurospheres showed reduced proliferation rate when compared to $Mri^{+/+}$ controls.

2. Materials and Methods

2.1. Mouse models

All experiments involving mice were performed according to the protocols approved by the Animal Resources Care Facility of Norwegian University of Science and Technology (NTNU, Norway). $Ung^{-/-}$ mice were described previously [32]. $Mri^{+/-}$ mice were generated on request and described here for the first time.

2.2. Generation of $Mri^{+/-}$ mice

MRI-deficient ($Mri^{-/-}$) mice were generated through a CRISPR/Cas9 gene-editing approach in 2017 by Horizon Discovery (Saint Louis, USA) upon request from the Oksenych group (IKOM, Faculty of Medicine and Health Science, NTNU, Norway). Single-guide RNA (sgRNA) GGG CTG TCA TCC AAG AGG GGA GG was designed to target *exon 2* of *Mri* gene in C57BL/6 mice. The 14 bp deletion resulted in a premature stop codon (Figure 1A). Cas9 and sgRNAs were injected into single-cell fertilized embryos, which were then transferred back into pseudopregnant females for gestation. Live-born pups were screened for indel mutation by DNA sequencing. Homozygous pups were used for back-crossing with wild type C57BL/6 mice. Heterozygous $Mri^{+/-}$ mice were obtained from Horizon Discovery.

Peer-reviewed version available at Biomolecules 2019, 9, 798; doi:10.3390/biom9120798

2.3. Mouse genotyping

Two polymerase chain reactions (PCRs) were designed to determine mouse genotypes. The first PCR was performed using TCAGGTCTGCCCTACACTGA and GTGGTGGTGCTTCTCTGTGA primers, detecting both wild type (428 bp) and null (414 bp) alleles (Figure 1B). The second PCR performed with TCAGGTCTGCCCTACACTGA and AGAGGGGAGGACCC primers was used to validate the presence of the WT allele (234 bp, Figure 1B). The PCRs were performed using 50 ng of genomic DNA extracted from murine tissues (e.g., ears, tails), in a final reaction volume of 25 µL, using the Taq 2x Master Mix Kit (New England Biolabs® Inc., Ipswich, Massachusetts, USA; #M0270L). The 2.5% agarose gel was used to separate 428 bp and 414 bp PCR products during 18 h at 4°C, 90 V; 0.7% agarose gel was used to detect 234 bp PCR product (75 min, room temperature, 124 V). Genomic DNA isolated from *Mri*$^{+/+}$ and *Mri*$^{-/-}$ cells, as well as samples with no genomic DNA, were used as PCR controls (Figure 1B).

2.4. Fluorescence-activated cell sorting, splenocyte and thymocyte count

Fluorescence-activated cell sorting (FACS) analysis was performed as previously described [12, 33]. Briefly, spleens and thymi were isolated from 2-month-old mice, splenocytes and thymocytes were counted using Countess™ Automated Cell Counter (Invitrogen); the cell suspension was spun down and diluted with PBS to get a final cell concentration of 2.5 x 10^7/mL. The samples of 2.5 x 10^6 splenocytes or thymocytes were blocked for 15 minutes at room temperature with Mouse BD fragment crystallizable (Fc) Block™ (1:50 dilution) (BD Biosciences, Franklin Lakes, New Jersey, USA; #553142). The cells were then incubated with fluorochrome-conjugated antibodies (see below) and sorted.

2.5. Class switch recombination

Class switch recombination (CSR) from IgM to IgG1 was performed as previously described [12]. Naïve B lymphocytes were purified from spleens of 2-month-old mice, using EasySep mouse B cell enrichment kit (STEMCELL Technology, Vancouver, Canada; #19854) according to the manufacturers' instructions. For each CSR assay, 2 x 10^4 cells/200 µL were used in duplicates. The cells were stimulated with LPS (Lipopolysaccharides, 40 µg/ml; Sigma Aldrich, St. Louis, MO, USA; #437627-5MG) and IL-4 (Interleukin 4, 20 ng/ml; PeproTech, Stockholm, Sweden; #214-14) for 96 h. Then the cells were blocked with Fc receptor antibody (2.4G2) and normal mouse serum (Invitrogen, Carlsbad, California, USA; #10410). The cells were washed in PermWash™ (BD Biosciences, New Jersey, USA; #554723). Intracellular staining was done using fluorescently tagged anti-mouse antibodies (IgG1-APC) (BioLegend, San Diego, USA; #406610) and the succeeding wash was performed in PermWash. The cells were resuspended in 300 µl of CellFix (BD Biosciences, New Jersey, USA; #340181). Viable CD19$^+$ B lymphocytes were analyzed for IgG1 expression using FlowJo® (Ashland, Oregon, USA) version 7.6 for Windows.

2.6. Double strand break sensitivity assay

DSBs sensitivity assay was performed as previously described [11, 33, 34]. Human nearly-haploid HAP1 cells were generated by Horizon Discovery Group (Waterbeach, UK, #HZGHC005061c001 and #HZGHC005061c004) and are commercially available. HAP1 cells were cultured according to the manufacturer's instructions. Doxorubicin (Selleckchem, Houston, TX, USA; #S1208), bleomycin (Selleckchem; #S1214) and etoposide (Sigma-Aldrich, USA; #E1383) were used to induce DSBs, and PrestoBlue™ Cell Viability Reagent (Thermo Fisher, USA; #A13262) was used to estimate cellular metabolism levels. Briefly, 2000 cells per well were seeded into 96-well plates, in 100 µL of IMDM medium (day 0). On day 1, 50 µL of the medium was replaced with 50 µL of fresh medium containing doxorubicin, bleomycin or etoposide, when indicated. Each experimental condition was performed in triplicates. On day 4, 11 µL of 10x PrestoBlue reagent was added to the wells and incubated for 30 min at 37°C. The cellular viability was estimated according to manufacturer's instructions, using the excitation/emission wavelengths set at 544/590 nm.

Peer-reviewed version available at Biomolecules 2019, 9, 798; doi:10.3390/biom9120798

2.7. Brain isolation and neural stem progenitor cell culture

The brain was isolated from postnatal day one mouse after the cerebellum was removed. The isolated brain was mechanically disrupted in proliferation medium consisting of Dulbecco Modified Eagle Medium, Nutrient Mixture F12 (DMEM/F12; Thermo Fisher, USA; #11330-057), supplemented with penicillin/streptomycin (Thermo Fisher, USA; #15140122), B27 without vitamin A (Thermo Fischer Scientific, USA; #12587001), EGF (10 ng/ml; PeproTrech, Stockholm, Sweden; #AF-100-15) and bFGF (20ng/ml; PeproTech; #100-18B). Neural stem progenitor cells (NSPC) form free-floating globular structures referred to as neurospheres. The neurospheres were formed during the incubation at 37°C, 5% CO_2 and 95% humidity in order to perform proliferation and self-renewal assay (Figure 3A) [35].

2.8. Neural stem progenitor cell proliferation and self-renewal assays

Early passage NSPCs (P3–P10) were used throughout all the NSPC experiments. A PrestoBlue™ Cell Viability Assay was used to investigate the neurosphere proliferation rates, following the manufacturer's instructions during each incubation day 1 to 7. The capacity of neural stem cells to maintain their multipotency *ex vivo* was assessed by determining the number and two-dimensional size of neurospheres [35]. Single NSPCs were plated onto 6-well suspension plates in the proliferation medium on day 0. During days 8 and 10 in culture, images of the entire wells were captured using EVOS microscope. Only areas between 50 and 1500 pixels were included in the analyses.

2.9. Antibodies

The following antibodies were used for FACS. Rat anti-mouse anti-CD16/CD32 (Fc Block, BD Biosciences, USA; #553141, 1 : 50); anti-CD4-PE-Cy7 (Thermo Scientific, USA, #25-0042-81, 1 : 100); anti-CD8-PE-Cy5 (BD Biosciences, USA, #553034, 1 : 100); anti-CD19-PE-Cy7 (Biolegends, USA, #115520, 1 : 100). Hamster anti-mouse anti-CD3-APC (Biolegends, USA, #100312, 1 : 100).

3. Results

3.1. Generation of *Mri*$^{-/-}$ mice

To investigate the impact of Mri on mouse development, we generated a mouse model with 14 bp frame-shift deletion in *Mri exon 2* on a C57BL/6 background (Figure 1A). Purified sgRNA and Cas9 RNA were introduced to fertilized oocytes, resulting in complete inactivation of the *Mri* gene. *Mri* status (WT, wild type, +/+; heterozygous, +/-; and null, -/-) was confirmed for every experiment by PCR screening (Figure 1B). *Mri*$^{+/+}$, *Mri*$^{+/-}$ and *Mri*$^{-/-}$ mice were born from *Mri*$^{+/-}$ parents at ratios close to 1: 2: 1 (Figure 1C). Thirty-day old *Mri*$^{-/-}$ mice possessed an average body weight of 15.0 g, which was slightly lower but not significantly different from *Mri*$^{+/+}$ controls, with a bodyweight of 17.5 g, on average (Figure 1D). The lifespan of *Mri*$^{-/-}$ and *Mri*$^{+/-}$ mice was monitored for up to 12 months, according to the local regulations. During this time frame, both *Mri*$^{-/-}$ and *Mri*$^{+/-}$ mice were fertile and had no cancer incidence, similarly to the *Mri*$^{+/+}$ controls.

Preprints (www.preprints.org) | NOT PEER-REVIEWED | Posted: 24 November 2019 doi:10.20944/preprints201911.0292.v1

Peer-reviewed version available at Biomolecules 2019, 9, 798; doi:10.3390/biom9120798

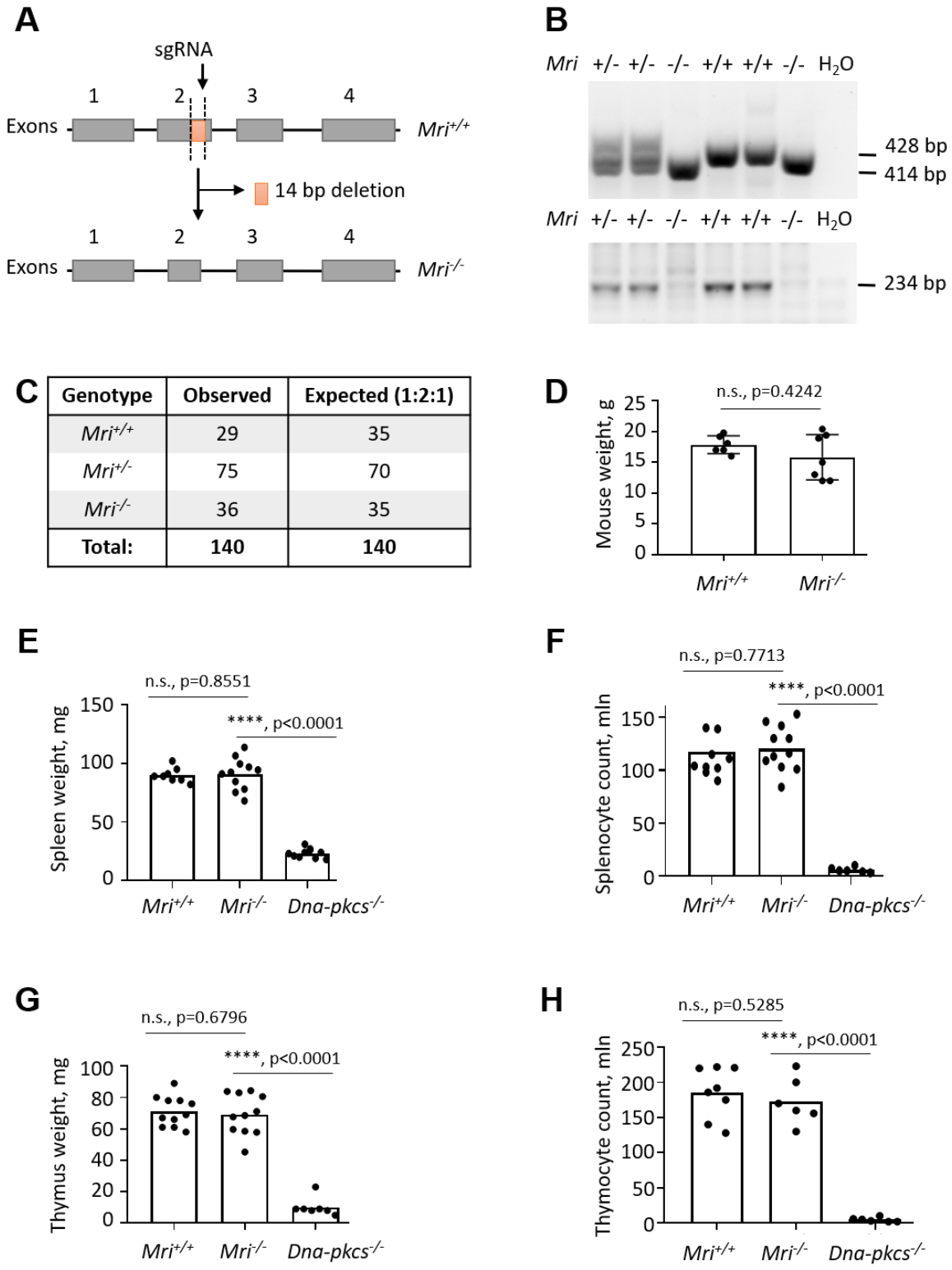

Genotype	Observed	Expected (1:2:1)
Mri$^{+/+}$	29	35
Mri$^{+/-}$	75	70
Mri$^{-/-}$	36	35
Total:	**140**	**140**

Figure 1. Generation of *Mri*$^{-/-}$ mice. **(A)** Top. Schematic diagram of murine *Mri* locus indicating the frame-shift mutation in the *exon 2*, induced by the sgRNA and resulting in a 14 bp deletion. Bottom. Resulting *Mri*$^{-/-}$ locus lacking part of the *exon 2*. **(B)** Top. PCR-based genotyping strategy reveals the *Mri* WT allele (428 bp) and *Mri* null allele (414 bp). Bottom. WT gene validation PCR reveals the *Mri* wild type allele (234 bp). **(C)** Analyses of 140 pups born from *Mri*$^{+/-}$ parents reveals expected genetic distribution of *Mri*$^{+/+}$ (29), *Mri*$^{+/-}$ (75) and *Mri*$^{-/-}$ (36) mice, which is close to the Mendelian distribution 1: 2: 1. **(D)** Body weight of six to eight week old *Mri*$^{+/+}$ mice (n=6) is not distinguishable from *Mri*$^{-/-}$ mice (n=7), p=0.4242. **(E)** The weight of spleens isolated from *Mri*$^{+/+}$ (n=8) and *Mri*$^{-/-}$ mice (n=11) is not

significantly different, p=0.8551. Spleen size in immunodeficient *Dna-pkcs*$^{-/-}$ mice (n=10) is reduced when compared to the *Mri*$^{+/+}$ and *Mri*$^{-/-}$ mice, p<0.0001. **(F)** Splenocyte count is not affected in the *Mri*$^{-/-}$ mice (n=11) when compared to the *Mri*$^{+/+}$ (n=10), p=0.7713. A number of splenocytes in immunodeficient *Dna-pkcs*$^{-/-}$ mice (n=6) is significantly reduced when compared to *Mri*$^{+/+}$and *Mri*$^{-/-}$ mice, p<0.0001. **(G)** The weight of thymus from *Mri*$^{+/+}$ (n=11) and *Mri*$^{-/-}$ (n=11) mice is similar, p=0.6796. Thymus size in immunodeficient *Dna-pkcs*$^{-/-}$ mice (n=7) is significantly reduced when compared to *Mri*$^{+/+}$and *Mri*$^{-/-}$ mice, p<0.0001. **(H)** Thymocyte count is nearly identical in *Mri*$^{+/+}$ (n=8) and *Mri*$^{-/-}$ (n=6) mice, p=0.5285. A number of thymocytes in immunodeficient *Dna-pkcs*$^{-/-}$ mice (n=6) is significantly reduced when compared to *Mri*$^{+/+}$and *Mri*$^{-/-}$ mice, p<0.0001.

3.2. Mri$^{-/-}$ *mice develop normal spleens and thymi*

The NHEJ is required for the V(D)J recombination in developing B and T lymphocytes, and for CSR in mature B cells [1]. To determine specific functions of Mri in B and T cell development, we first analyzed spleens and thymi isolated from Mri-deficient and WT mice. The average weights of spleens (91 mg) and thymi (69 mg), as well as average count of splenocytes (121 million) and thymocytes (173 million), was not affected in *Mri*$^{-/-}$ mice when compared to *Mri*$^{+/+}$ controls (90 mg; 71 mg; 118 million; 186 million, respectively). These numbers were significantly different from immunodeficient controls, *Dna-pkcs*$^{-/-}$ mice (23 mg; 10 mg; 6 million; 5 million, respectively) (Figure 1E-H). Moreover, proportions of CD19^{+} B cells in spleens of six to eight weeks old *Mri*$^{-/-}$ mice were on average 60%, which was similar to the proportion of CD19^{+} in *Mri*$^{+/+}$ mice (55%, p=0.0668), and significantly higher than background levels detected in immunodeficient *Dna-pkcs*$^{-/-}$ controls (p<0.0001; Figure 2A). The average proportion of CD3^{+} T splenocytes in *Mri*$^{-/-}$ mice (21%) was also similar to the one observed in *Mri*$^{+/+}$ controls (22%, p=0.8228), and higher than in *Dna-pkcs*$^{-/-}$ controls (1%, p<0.0001; Figure 2A). *Mri*$^{+/+}$ and *Mri*$^{-/-}$ mice had similar proportions of CD4^{+} T cells (p=0.8876) and CD8^{+} T cells (p=0.7026) in the spleens, while proportions of CD4^{+} and CD8^{+} T splenocytes in *Dna-pkcs*$^{-/-}$ controls were 4-5 folds reduced (p<0.0001, Figure 2B). In thymi of six- to eight-week-old *Mri*$^{+/+}$ and *Mri*$^{-/-}$ mice, proportions of CD4^{+}, CD8^{+} and CD4^{+}CD8^{+} T cells was similar (p>0.5589), while only background levels were detected in *Dna-pkcs*$^{-/-}$ controls (p<0.0001, Figure 2C).

3.3. CSR to IgG1 is reduced in Mri$^{-/-}$ *mice.*

To determine whether Mri deficiency affects CSR, we isolated B cells from the spleens of *Mri*$^{+/+}$ and *Mri*$^{-/-}$ mice and stimulated the cells with LPS and IL-4. After 96 h, we detected that average IgG1 levels were 33% in *Mri*$^{-/-}$ mice, which was significantly lower (p=0.0031) than in *Mri*$^{+/+}$ controls (average 39%; Figure 2D). B lymphocytes isolated from *Ung*$^{-/-}$ mice were used as negative control and possessed on average only 2% of IgG1 at the end of the experiment (96 h), which is lower than in *Mri*$^{+/+}$ or *Mri*$^{-/-}$ mice (p<0.0001).

Preprints (www.preprints.org) | NOT PEER-REVIEWED | Posted: 24 November 2019 doi:10.20944/preprints201911.0292.v1

Peer-reviewed version available at Biomolecules 2019, 9, 798; doi:10.3390/biom9120798

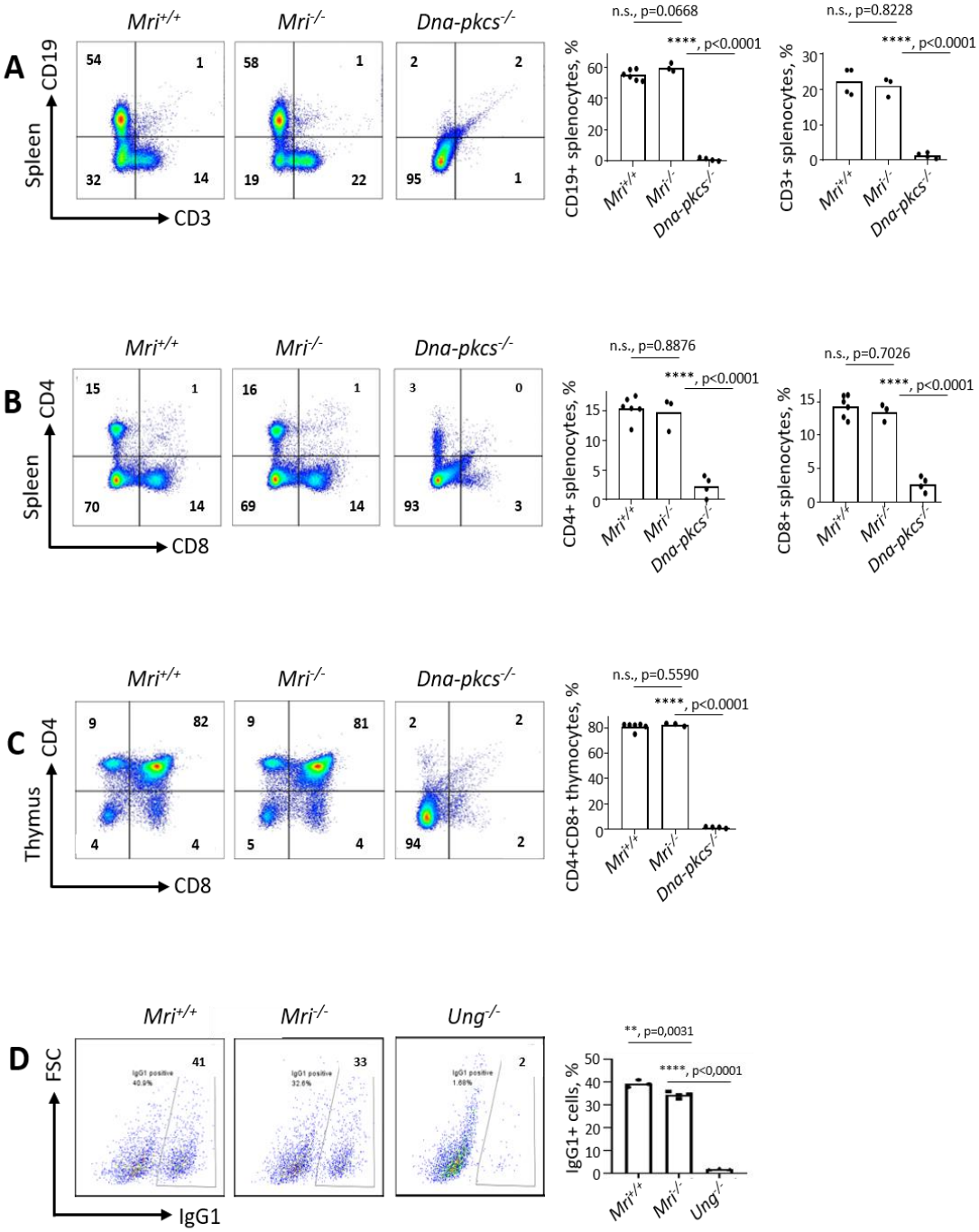

Figure 2. Lymphocyte development in *Mri*$^{-/-}$ mice. **(A)** Proportions of T (CD3^{+}) and B (CD19^{+}) cells in the spleens of *Mri*$^{+/+}$ (n=6), *Mri*$^{-/-}$ (n=3) and *Dna-pkcs*$^{-/-}$ (n=4) mice. Proportions of T and B cells are similar in *Mri*$^{+/+}$ and *Mri*$^{-/-}$ mice, p>0.0667, and are only background levels in immunodeficient *Dna-pkcs*$^{-/-}$ mice, p<0.0001. **(B)** Proportions of CD4^{+} and CD8^{+} T splenocytes in *Mri*$^{+/+}$ (n=6), *Mri*$^{-/-}$ (n=3) and *Dna-pkcs*$^{-/-}$ (n=4) mice. *Mri*$^{-/-}$ mice possess similar proportions of CD4^{+} T helper and CD8^{+} T cytotoxic cells when compared to *Mri*$^{+/+}$ mice, p=0.8876 and p=0.7026, respectively. Only background levels of CD4^{+} and CD8^{+} T cells are present in immunodeficient *Dna-pkcs*$^{-/-}$ spleens, p<0,0001. **(C)** Proportions of CD4^{+}, CD8^{+} and CD4^{+}CD8^{+} thymocytes in *Mri*$^{+/+}$ (n=6), *Mri*$^{-/-}$ (n=3) and *Dna-pkcs*$^{-/-}$ (n=4) mice. Proportions of T cell types in *Mri*$^{-/-}$ mice are similar to the ones detected in *Mri*$^{+/+}$ mice, p>0.5589 and higher than in *Dna-pkcs*$^{-/-}$ mice, p<0.0001. **(D)** CSR to IgG1 in primary B splenocytes isolated from the *Mri*$^{-/-}$ mice (n=4) is reduced when compared to the cells from the *Mri*$^{+/+}$ mice (n=3), p=0.0032. CSR to IgG1 was significantly reduced in *Ung*$^{-/-}$ B cells (n=3) when compared to the *Mri*$^{+/+}$ and *Mri*$^{-/-}$, p<0.0001.

Peer-reviewed version available at Biomolecules 2019, 9, 798; doi:10.3390/biom9120798

3.4. Lack of Mri results in the reduced proliferation rate of neuronal stem progenitor cells

Previous studies have shown that single knockout of NHEJ DNA repair genes, e.g. *Xrcc4*, *Lig4*, *Ku70*, results in impaired nervous system development in mice [4, 14, 15]. To determine the impact of Mri on the developing nervous system, we used NSPC isolated from $Mri^{+/+}$ and $Mri^{-/-}$ mice at postnatal day 1. We performed four independent experiments using two cell lines from two mice of each genotype. The average proliferation rate of $Mri^{-/-}$ neurospheres was approximately 35% lower than that in WT controls, p=0.0043 (Figure 3B).

3.5. Normal self-renewal capacity of Mri-deficient neuronal stem progenitor cells

To analyze the capacity of NSPCs to maintain features of stem cells throughout cell divisions and numerous propagations (self-renewal capacity), we counted the number of neurospheres formed in cell culture. In four independent experiments, we plated 10,000 single NSPCs and cultured for 8 days. In total, we counted 5123 neurospheres that originated from $Mri^{+/+}$, and 4608 from $Mri^{-/-}$ mice. On average, there were 256 neurospheres in each of 20 $Mri^{+/+}$ samples analyzed, and 230 neurospheres in each of 20 $Mri^{-/-}$ samples (p=0.7254, n.s., Figure 3C). In addition, the images of neurospheres were collected and the surface was calculated using *ImageJ* software. Inactivation of *Mri* did not affect the average diameter of neurospheres, which was 461 px² on average in $Mri^{+/+}$ and 427 px² in $Mri^{-/-}$ neurospheres, p=0.4915 (Figure 3D). We concluded that Mri is dispensable for the self-renewal capacity of NSPC.

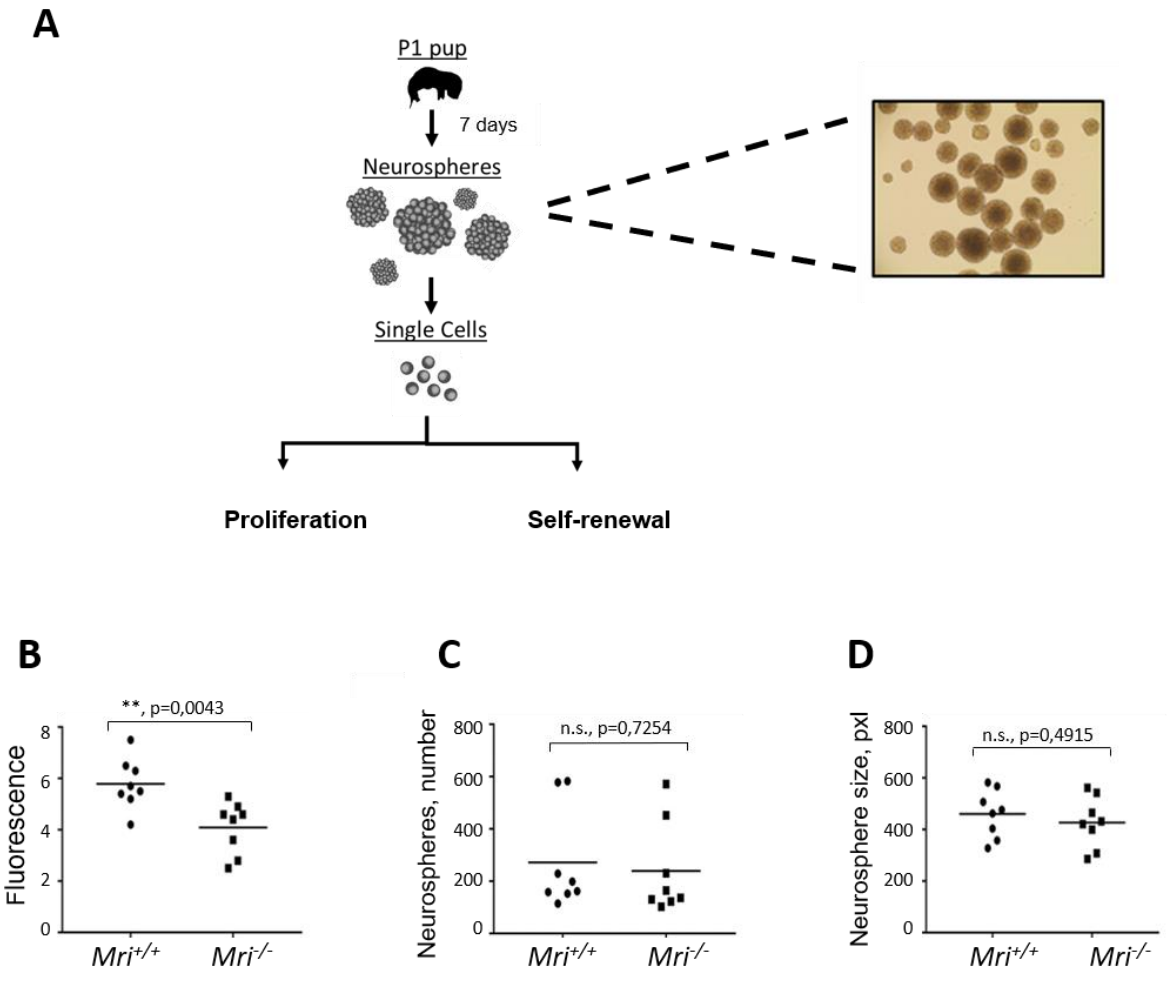

Figure 3. Characterization of neurogenesis in $Mri^{-/-}$ mice. For each experiment, four independent cell lines isolated from two mice were used (n=8). **(A)** Neurospheres isolation diagram from $Mri^{+/+}$ and $Mri^{-/-}$ mice at postnatal day 1. **(B)** Neurospheres proliferation isolated from the $Mri^{-/-}$ mice is reduced when compared to

Preprints (www.preprints.org) | NOT PEER-REVIEWED | Posted: 24 November 2019 doi:10.20944/preprints201911.0292.v1

Peer-reviewed version available at Biomolecules 2019, 9, 798; doi:10.3390/biom9120798

the *Mri*$^{+/+}$ mice, p=0.0043. **(C)** Number of neurospheres formed in cell culture for 8 days. *Mri*$^{-/-}$ and *Mri*$^{+/+}$ neurospheres possess similar self-renewal capacity, p=0.7254. **(D)** Neurosphere size isolated from *Mri*$^{-/-}$ and *Mri*$^{+/+}$ mice are similar, p=0.4915. The surface of neurospheres, pxl. Areas between 50 and 1500 pixels were included in the analyses. Four independent experiments using two cell lines of each genotype were performed in all experiments (A-C). p values were calculated using unpaired t-test. The horizontal bars represent the average.

3.6. Human HAP1 cells lacking Mri possess normal levels of sensitivity to DSBs

Deficiency for XRCC4, LIG4, XLF, or DNA-PKcs results in hypersensitivity to DSBs in human HAP1 cells [11, 33, 34]. To determine the effect of Mri on DSB sensitivity, we obtained two independent clones of *MRI*-deficient HAP1 cells, as well as WT and *XRCC4*-deficient controls. We exposed the HAP1 cells to DSB-inducing agents bleomycin (0 to 0.4 μM), doxorubicin (0 to 4 nM) and etoposide (0 to 160 nM), and evaluated the cell viability 4 days later (Figure 4). We observed no hypersensitivity of HAP1 cells lacking Mri when compared to WT controls. However, cells lacking XRCC4 were hypersensitive to all indicated compounds, bleomycin, doxorubicin, and etoposide (p<0.0001, Figure 4).

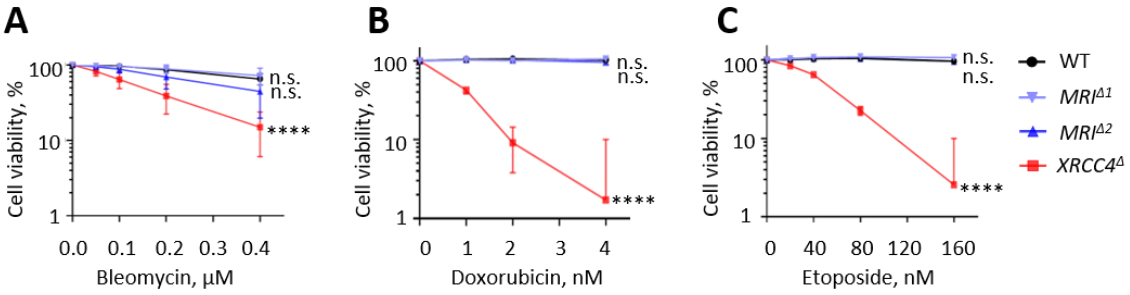

Figure 4. Sensitivity to DSBs in *Mri*-deficient HAP1 cells. Sensitization of WT, two independent Mri-deficient clones, *MRI*$^{\Delta 1}$ and *MRI*$^{\Delta 2}$, and *XRCC4*$^{\Delta}$ HAP1 cells to bleomycin **(A)**, doxorubicin **(B)**, and etoposide **(C)** at indicated concentrations. Results are from the mean (SD) of three repeats. Cell viability (%) represents the relative proportion of the fluorescence normalized to untreated cells. Comparisons between every two groups were made using one-way ANOVA, GraphPad Prism 8. WT, *MRI*$^{\Delta 1}$ and *MRI*$^{\Delta 2}$ vs *XRCC4*$^{\Delta}$, p<0.0001 (****); WT vs *MRI*$^{\Delta 1}$, p=0.9983 (n.s); WT vs *MRI*$^{\Delta 2}$, p=0.1295 (n.s); *MRI*$^{\Delta 1}$ vs *MRI*$^{\Delta 2}$, p=0.1791 (n.s).

4. Discussion

We have generated a new knockout mouse model with 14 bp deletion in *exon 2* of the *Mri* gene, *Mri*$^{-/-}$. While we were characterizing our mouse model, another group reported an independently-generated *Mri*-deficient mouse [21], which possessed a similar phenotype. Thus, our observations are confirmatory to the findings observed by the Sleckman group [21].

The mice lacking Mri are live-born at expected ratios and demonstrate normal growth and development of lymphoid organs. *Mri*$^{-/-}$, *Mri*$^{+/-}$ and *Mri*$^{+/+}$ mice possess similar sizes of spleens and thymi, a similar number of splenocytes and thymocytes, and proportions of B and T cells (Figure 1). Similarly to Mri-deficient mice, *Paxx*$^{-/-}$ mice did not have detectable phenotype [9-13]. However, inactivation of other NHEJ factors resulted in reduced number of B and T cells (*Xlf*$^{-/-}$ mice, [5-8, 19, 22, 24]), block in B and T cell development, e.g. *Artemis*$^{-/-}$ [36], *Dna-pkcs*$^{-/-}$ [37], *Ku70*$^{-/-}$ [38], *Ku80*$^{-/-}$ [39]; or even embryonic lethality in *Xrcc4*$^{-/-}$ [40] and *Lig4*$^{-/-}$ [41].

The CSR to IgG1 was reduced in primary B cells isolated from *Mri*$^{-/-}$ mice when compared to WT controls (Figure 2), which suggests that Mri is involved in specific DNA repair-mediated event. Furthermore, we isolated neuronal stem progenitor cells from *Mri*$^{-/-}$ brains and found that these cells proliferate slower when compared to *Mri*$^{+/+}$ controls. Reduced proliferation rates of Mri-deficient neuronal stem progenitor cells could be explained, as one option, by lower expression or lack of factors functionally redundant with Mri in these cell types. Future studies would be required to address this option. Moreover, future studies may address questions such as neurological defects and

Peer-reviewed version available at Biomolecules 2019, 9, 798; doi:10.3390/biom9120798

cognitive functions in mice lacking Mri, as well as whether the Mri-deficient mice are prone to infections.

In addition, we found that human nearly haploid HAP1 cell lines lacking Mri possessed no proliferation defect or hypersensitivity to DNA damaging agents, such as etoposide, doxorubicin and bleomycin (Figure 4). Previously, it was reported that murine embryonic fibroblasts (MEF) lacking Mri are hypersensitive to ionizing radiation when compared to WT controls, although the sensitivity is less obvious than in XLF-deficient MEFs [21]. The discrepancy between our and previously published data could be due to the usage of different cell types, difference between species, as well as distinct ways to induce DNA damages (e.g., chemicals vs irradiation). Further studies involving various cell type models originated from different species, and using various DNA damaging strategies, would deepen our understanding of the specific functions of Mri in DNA repair in mammalian cells. Overall, we concluded that the lack of Mri has rather a minor effect on murine and human cells.

Combined inactivation of *Mri* and *Xlf* [21], however, revealed an important role of Mri in mouse development, which was overlooked due to its functional redundancy with XLF. Synthetic lethality between *Mri* and *Xlf* complicated studies of genetic interaction between these factors *in vivo*. There are several potential ways to overcome this challenge. One option is to use conditional knockouts of *Xlf* or *Mri* genes. Moreover, there might be another genetic-based approach. Inactivation of one or two alleles of *Trp53* partially rescued synthetic lethality between *Xlf* and *Dna-pkcs* [11, 19, 20] and *Xlf* and *Paxx* [11]. In addition, deficiency or haploinsufficiency for *Trp53* rescued embryonic lethality of *Lig4*$^{-/-}$ and *Xrcc4*$^{-/-}$ mice [14, 15]. Inactivation of the *Atm* gene rescued embryonic lethality of *Lig4*$^{-/-}$ mice [42]. Finally, inactivation of both alleles of *Ku80* rescued embryonic lethality of *Lig4*$^{-/-}$ mice [18], and inactivation of *Ku70* rescued synthetic lethality between *Xlf* and *Dna-pkcs* [20]. Based on these data, one can speculate that inactivation of *Trp53*, *Atm*, *Ku70* or *Ku80* will rescue synthetic lethality between *Xlf* and *Mri*. Moreover, given critical roles of Ku70 and Ku80 in initiation of classical NHEJ, one could propose that mice lacking all known NHEJ factors, e.g. *Ku70*$^{-/-}$*Ku80*$^{-/-}$*Dna-pkcs*$^{-/-}$*Artemis*$^{-/-}$*Xlf*$^{-/-}$*Paxx*$^{-/-}$*Mri*$^{-/-}$*Xrcc4*$^{-/-}$*Lig4*$^{-/-}$ will be viable, indistinguishable from Ku-deficient mice, and serve as a suitable *in vivo* model to investigate alternative end-joining, A-EJ.

5. Conclusions

A new *Mri*-deficient mouse model was generated. *Mri*-deficient mice possessed normal body size and number of B and T lymphocytes; however, Mri is required for efficient class switch recombination process in mature B cells. *Mri*$^{-/-}$ neurospheres showed reduced proliferation rate, but similar self-renewal capacity, when compared to *Mri*$^{+/+}$ controls.

Author Contributions: V.O. designed and performed experiments, contributed key reagents and analyzed the data. A.S. performed CSR assay using primary B cells. MT.X. performed DSBs sensitivity assay using human HAP1 cells. S.CZ., C.H., Ø.R., Q.Z., A.L., J.W., NB.L. performed lymphocyte analyzes. Ø.R., W.W., and P.J. performed and analyzed neurosphere-based experiments. R.GF developed *Mri*$^{-/-}$ genotyping strategy. M.B. and V.O. interpreted the results. The paper was written by Ø.R., S.CZ. and V.O.; all the authors read and approved the manuscript.

Funding: This work was supported by the Research Council of Norway Young Talent Investigator grant (# 249774) to VO. In addition, VO group was supported by the Liaison Committee for education, research and innovation in Central Norway (# 13477), the Norwegian Cancer Society (# 182355), FRIMEDBIO grants (# 270491 and # 291217), and The Outstanding Academic Fellow Program at NTNU (2017-2021). JW is supported by Erasmus mobility program.

Acknowledgments: We gratefully acknowledge support by Molecular Imaging Core Facility (CMIC) and Comparative Medicine Core Facility (CoMed) at the Faculty of Medicine and Health Sciences, NTNU (Trondheim).

Conflicts of Interest: The authors declare no conflict of interest.

Abbreviations:

ATM	Ataxia-telangiectasia mutated
CSR	Class switch recombination
DDR	DNA damage response
DNA-PKcs	DNA-dependent protein kinase
DSBs	DNA double-strand breaks
GFAP	Glial fibrillary acid protein
HAP1	A near-haploid human cell line derived from KBM-7 cell line
IL-4	Interleukin 4
Lig4	DNA ligase IV
LPS	Lipopolysaccharides
Mri	Modulator of retroviral infection
NHEJ	Non-homologous end-joining
NSPC	Neuronal stem progenitor cells
PAXX	Paralogue of XRCC4 and XLF
PCR	Polymerase chain reaction
XLF	XRCC4-like factor
XRCC4	X-ray repair cross-complementing protein 4

References

1. Kumar, V., F.W. Alt, and V. Oksenych, *Functional overlaps between XLF and the ATM-dependent DNA double strand break response.* DNA Repair (Amst), 2014. **16**: p. 11-22. DOI: 10.1016/j.dnarep.2014.01.010
2. Pannunzio, N.R., G. Watanabe, and M.R. Lieber, *Nonhomologous DNA end-joining for repair of DNA double-strand breaks.* J Biol Chem, 2018. **293**(27): p. 10512-10523. DOI: 10.1074/jbc.TM117.000374
3. Scully, R., et al., *DNA double-strand break repair-pathway choice in somatic mammalian cells.* Nat Rev Mol Cell Biol, 2019. DOI: 10.1038/s41580-019-0152-0
4. Kumar, V., F.W. Alt, and V. Oksenych, *Reprint of "Functional overlaps between XLF and the ATM-dependent DNA double strand break response".* DNA Repair (Amst), 2014. **17**: p. 52-63. DOI: 10.1016/j.dnarep.2014.04.004
5. Li, G., et al., *Lymphocyte-specific compensation for XLF/cernunnos end-joining functions in V(D)J recombination.* Mol Cell, 2008. **31**(5): p. 631-40. DOI: 10.1016/j.molcel.2008.07.017
6. Vera, G., et al., *Cernunnos deficiency reduces thymocyte life span and alters the T cell repertoire in mice and humans.* Mol Cell Biol, 2013. **33**(4): p. 701-11. DOI: 10.1128/MCB.01057-12
7. Zha, S., et al., *ATM damage response and XLF repair factor are functionally redundant in joining DNA breaks.* Nature, 2011. **469**(7329): p. 250-4. DOI: 10.1038/nature09604
8. Oksenych, V., et al., *Functional redundancy between repair factor XLF and damage response mediator 53BP1 in V(D)J recombination and DNA repair.* Proc Natl Acad Sci U S A, 2012. **109**(7): p. 2455-60. DOI: 10.1073/pnas.1121458109
9. Abramowski, V., et al., *PAXX and Xlf interplay revealed by impaired CNS development and immunodeficiency of double KO mice.* Cell Death Differ, 2018. **25**(2): p. 444-452. DOI: 10.1038/cdd.2017.184
10. Balmus, G., et al., *Synthetic lethality between PAXX and XLF in mammalian development.* Genes Dev, 2016. **30**(19): p. 2152-2157. DOI: 10.1101/gad.290510.116
11. Castaneda-Zegarra, S., et al., *Synthetic lethality between DNA repair factors Xlf and Paxx is rescued by inactivation of Trp53.* DNA Repair (Amst), 2019. **73**: p. 164-169. DOI: 10.1016/j.dnarep.2018.12.002
12. Gago-Fuentes, R., et al., *Normal development of mice lacking PAXX, the paralogue of XRCC4 and XLF.* FEBS Open Bio, 2018. **8**(3): p. 426-434. DOI: 10.1002/2211-5463.12381
13. Liu, X., et al., *PAXX promotes KU accumulation at DNA breaks and is essential for end-joining in XLF-deficient mice.* Nat Commun, 2017. **8**: p. 13816. DOI: 10.1038/ncomms13816

14. Frank, K.M., et al., *DNA ligase IV deficiency in mice leads to defective neurogenesis and embryonic lethality via the p53 pathway.* Mol Cell, 2000. **5**(6): p. 993-1002.
15. Gao, Y., et al., *Interplay of p53 and DNA-repair protein XRCC4 in tumorigenesis, genomic stability and development.* Nature, 2000. **404**(6780): p. 897-900. DOI: 10.1038/35009138
16. Boboila, C., et al., *Alternative end-joining catalyzes robust IgH locus deletions and translocations in the combined absence of ligase 4 and Ku70.* Proc Natl Acad Sci U S A, 2010. **107**(7): p. 3034-9. DOI: 10.1073/pnas.0915067107
17. Boboila, C., et al., *Alternative end-joining catalyzes class switch recombination in the absence of both Ku70 and DNA ligase 4.* J Exp Med, 2010. **207**(2): p. 417-27. DOI: 10.1084/jem.20092449
18. Karanjawala, Z.E., et al., *The embryonic lethality in DNA ligase IV-deficient mice is rescued by deletion of Ku: implications for unifying the heterogeneous phenotypes of NHEJ mutants.* DNA Repair (Amst), 2002. **1**(12): p. 1017-26.
19. Oksenych, V., et al., *Functional redundancy between the XLF and DNA-PKcs DNA repair factors in V(D)J recombination and nonhomologous DNA end joining.* Proc Natl Acad Sci U S A, 2013. **110**(6): p. 2234-9. DOI: 10.1073/pnas.1222573110
20. Xing, M., et al., *Synthetic lethality between murine DNA repair factors XLF and DNA-PKcs is rescued by inactivation of Ku70.* DNA Repair (Amst), 2017. **57**: p. 133-138. DOI: 10.1016/j.dnarep.2017.07.008
21. Hung, P.J., et al., *MRI Is a DNA Damage Response Adaptor during Classical Non-homologous End Joining.* Mol Cell, 2018. **71**(2): p. 332-342 e8. DOI: 10.1016/j.molcel.2018.06.018
22. Lescale, C., et al., *RAG2 and XLF/Cernunnos interplay reveals a novel role for the RAG complex in DNA repair.* Nat Commun, 2016. **7**: p. 10529. DOI: 10.1038/ncomms10529
23. Chen, B.R., et al., *XLF and H2AX function in series to promote replication fork stability.* J Cell Biol, 2019. **218**(7): p. 2113-2123. DOI: 10.1083/jcb.201808134
24. Liu, X., et al., *Overlapping functions between XLF repair protein and 53BP1 DNA damage response factor in end joining and lymphocyte development.* Proc Natl Acad Sci U S A, 2012. **109**(10): p. 3903-8. DOI: 10.1073/pnas.1120160109
25. Alt, F.W., et al., *Mechanisms of programmed DNA lesions and genomic instability in the immune system.* Cell, 2013. **152**(3): p. 417-29. DOI: 10.1016/j.cell.2013.01.007
26. Yeap, L.S. and F.L. Meng, *Cis- and trans-factors affecting AID targeting and mutagenic outcomes in antibody diversification.* Adv Immunol, 2019. **141**: p. 51-103. DOI: 10.1016/bs.ai.2019.01.002
27. Alt, F.W. and B. Schwer, *DNA double-strand breaks as drivers of neural genomic change, function, and disease.* DNA Repair (Amst), 2018. **71**: p. 158-163. DOI: 10.1016/j.dnarep.2018.08.019
28. Agarwal, S., et al., *Isolation, characterization, and genetic complementation of a cellular mutant resistant to retroviral infection.* Proc Natl Acad Sci U S A, 2006. **103**(43): p. 15933-8. DOI: 10.1073/pnas.0602674103
29. Slavoff, S.A., et al., *A human short open reading frame (sORF)-encoded polypeptide that stimulates DNA end joining.* J Biol Chem, 2014. **289**(16): p. 10950-7. DOI: 10.1074/jbc.C113.533968
30. Grundy, G.J., et al., *The Ku-binding motif is a conserved module for recruitment and stimulation of non-homologous end-joining proteins.* Nat Commun, 2016. **7**: p. 11242. DOI: 10.1038/ncomms11242
31. Arnoult, N., et al., *Regulation of DNA repair pathway choice in S and G2 phases by the NHEJ inhibitor CYREN.* Nature, 2017. **549**(7673): p. 548-552. DOI: 10.1038/nature24023
32. Nilsen, H., et al., *Uracil-DNA glycosylase (UNG)-deficient mice reveal a primary role of the enzyme during DNA replication.* Mol Cell, 2000. **5**(6): p. 1059-65.

33. Dewan, A., et al., *Robust DNA repair in PAXX-deficient mammalian cells.* FEBS Open Bio, 2018. **8**(3): p. 442-448. DOI: 10.1002/2211-5463.12380
34. Xing, M. and V. Oksenych, *Genetic interaction between DNA repair factors PAXX, XLF, XRCC4 and DNA-PKcs in human cells.* FEBS Open Bio, 2019. DOI: 10.1002/2211-5463.12681
35. Wang, W., et al., *Mitochondrial DNA integrity is essential for mitochondrial maturation during differentiation of neural stem cells.* Stem Cells, 2010. **28**(12): p. 2195-204. DOI: 10.1002/stem.542
36. Rooney, S., et al., *Leaky Scid phenotype associated with defective V(D)J coding end processing in Artemis-deficient mice.* Mol Cell, 2002. **10**(6): p. 1379-90. DOI: 10.1016/s1097-2765(02)00755-4
37. Gao, Y., et al., *A targeted DNA-PKcs-null mutation reveals DNA-PK-independent functions for KU in V(D)J recombination.* Immunity, 1998. **9**(3): p. 367-76.
38. Gu, Y., et al., *Growth retardation and leaky SCID phenotype of Ku70-deficient mice.* Immunity, 1997. **7**(5): p. 653-65.
39. Nussenzweig, A., et al., *Requirement for Ku80 in growth and immunoglobulin V(D)J recombination.* Nature, 1996. **382**(6591): p. 551-5. DOI: 10.1038/382551a0
40. Gao, Y., et al., *A critical role for DNA end-joining proteins in both lymphogenesis and neurogenesis.* Cell, 1998. **95**(7): p. 891-902.
41. Frank, K.M., et al., *Late embryonic lethality and impaired V(D)J recombination in mice lacking DNA ligase IV.* Nature, 1998. **396**(6707): p. 173-7. DOI: 10.1038/24172
42. Sekiguchi, J., et al., *Genetic interactions between ATM and the nonhomologous end-joining factors in genomic stability and development.* Proc Natl Acad Sci U S A, 2001. **98**(6): p. 3243-8. DOI: 10.1073/pnas.051632098